Desalination and Water Treatment
www.deswater.com

doi: 10.5004/dwt.2019.23459

140 (2019) 103–117
February

Coupled transport phenomena of a bioswale process during storm runoff events: a CFD study using OpenFOAM

Joshua Lelemia Irvine[a], Albert S. Kim[a,*]

[a]*Department of Civil and Environmental Engineering, University of Hawaii at Manoa, 2540 Dole Street, Holmes Hall 383, Honolulu, Hawaii 96822, USA, Tel. +1 808 956 3718; Fax: +1 808 956 5014; emails: albertsk@hawaii.edu (A.S. Kim), joshuair@hawaii.edu (J.L. Irvine)*

Received 15 June 2018; Accepted 9 November 2018

ABSTRACT

Coupled transport phenomena within a bioswale are studied using the open-source computational fluid dynamics (CFD) software OpenFOAM. We investigated the unsteady behavior of momentum and mass transfer in a double-layered bioswale. To study the diffusive transport of a model pollutant, we developed a new solver, that we named interPhaseDiffusionFoam (https://github.com/enphysoft/interPhaseDiffusionFoam), which better mimics transport phenomena of non-volatile species at a phase boundary. We observed that heterogeneous infiltration patterns are strongly dependent upon stormwater runoff velocity, reverse air flow, and the presence of the drain pipe. The performance estimation and optimal design of a bioswale were thoroughly examined using 2D CFD simulations for a holistic understanding of coupled mass and momentum transport phenomena.

Keywords: Bioswale; Computational fluid dynamics; Low-impact development; Design optimization; Stormwater runoff; Stormwater pollution

1. Introduction

Modern urban development has resulted in noticeable hydrological alterations, especially near the boundaries between urban surfaces and natural ground [1]. Impervious surfaces consisting of stone, pavement, and roofing structures change hydrological and hydraulic flow patterns at a macroscopic scale. Stormwater runoff on impervious areas often causes urban flooding and, hence, leads to a deterioration in the respective ecosystem's functions [2,3]. Conventional structures for runoff management include roof gutters, storm sewers, and detention basins that are aimed to convey promptly stormwater runoff to off-site drain discharge locations. The continued increase in impervious areas will reduce natural porous surfaces to infiltrate rainfall and enhance the frequency and intensity of urban flooding [4–7].

Since the 1970s, onsite stormwater management approaches have been described by various technological terms, which include best management practices (BMPs) [8], green infrastructure [9], integrated urban water management (IUWM) [10,11], low-impact development (LID) [12–15], low-impact urban design and development [16], source control (SC) [17,18], stormwater control measures (SCMs) [19,20], sustainable urban drainage systems (SUDS) [21,22], sustainable drainage systems (SuDS) [23,24], and water sensitive urban design [25–28]. Thorough reviews of these terms can be found in work by Fletcher et al. [29] and Eckart et al. [30]. These management methods aim to retain the stormwater runoff with devices that emulate the natural hydrology before urbanization. One significant task when researching urban flooding mitigation is, per our investigation, the enhancement of onsite infiltration capability by increasing permeable catchment areas. Thereby, this paradigm shift from impervious to hybrid permeable surfaces has the potential to increase the threshold precipitation rate under which urban flooding begins within a certain lag time after a precipitation event starts. The hydraulic benefits of LID/BMP devices, however, cannot be fully attained without

---

* Corresponding author.

1944-3994/1944-3986

detailed analysis of the individual transport components at various scales.

Computational fluid dynamics (CFD) receives growing attention in the civil and environmental engineering field. This method can be used to enhance stormwater management design and optimize LID/BMP devices, especially at the conceptual stage of design development. CFD for LID/BMP applications possesses the following advantages. First, CFD provides an alternative cost-effective means to predict the complex transport phenomena of mass, momentum, energy, and especially chemical species in multi-phase LID/BMP devices. Second, CFD can model flow conditions when experimental tests are not easily reproducible because of limited environmental conditions for physical observations. In the case of LID/BMP, the various scenarios regarding stormwater runoff and pollutant transports are too immense and arduous to study experimentally. Finally, CFD provides much more detailed visualization as compared with analytical and experimental approaches. In analytical approaches, it is difficult to solve flow profiles in complex geometrical domains. Physical experimentation requires substantial resources, as well as cost and time to observe fluid flows and pollutant transport. In addition the quantitative description of fluid dynamic experiments does not provide complete data sets within available operating conditions. Using CFD, however, can evaluate and visualize the flow behavior over a range of parameters such as the flow speed and the hydraulic pressure. If CFD is well conducted within the design process, then LID/BMP systems can be optimized in terms of dimensions and cost. As a result, the unexpected effects of structural change could be identified and removed in early stages.

Limitations of CFD include inaccuracy of physical models, selection of appropriate boundary conditions, and unstable algorithms due to numerical errors. In the LID/BMP literature, software programs that model site-specific, sub-catchment scale systems are not CFD-based, which include Guelph All Weather Sequential Events Runoff (GAWSER) [31], Model for Urban Stormwater Improvement Conceptualization (MUSIC) [32–34], Soil Conservation Services (SCS) model using the curve number [35], Smart Growth Water Assessment Tool for Estimating Runoff (SG WATER) [36], Storm Water Management Model (SWMM) [6,37], Storm Water Management Model and Best Management Practice Decision Support System (SWMM-BMPDSS) [38,39], System for Urban Stormwater Treatment and Analysis Integration (SUSTAIN) [40], and MIKE SHE [41]. These macroscale fluid dynamics approaches do not originate from fundamental, microscopic transport mechanisms but employ approximate mass balances that often rely on experimental data. Thus, these approaches cannot identify local areas where ineffective operations of LID/BMP devices may occur.

In the practice of bioswale designs, guidelines and standards do not exist so as to provide optimal performance calculations during storm events. These design guides are not necessarily clear regarding proper specifications and bioswale hydraulic performance. For example, the Low Impact Development: A Practitioner's Guide for Hawaii [42] specifies the minimum requirements to design swales for various annual rainfall ranges. However, no detailed specifications exist regarding the proper sizing of underdrain pipes for swales. Similarly, guidelines for the states of Alaska [43] and Arizona [44] and the city of Las Vegas Valley, Nevada [45] offer qualitative descriptions for swale and bioretention systems, but these guidelines do not include methods to analyze pre-built LID/BMP structures. The BMP manual of Hawaii [46], as well as the technical guides from New Mexico [47], and Utah [48] adopted the rational method for peak runoff to design swale and bioretention systems, which was initially proposed by Prince George's County in 1993 [49]. Furthermore, the state of Washington requires the use of Manning's equation as a first approximation to obtain swale geometry [50]. The State of Oregon Manual [51], however, prescribes the bioswale sizing method based on the SCS quantification approach to treat a 24-hour storm event. In contrast, the state of California determines filter bed sizing using Darcy's Law [52], which was first developed by the city of Austin, Texas, in 1996 [53]. Finally, the Idaho Department of Environmental Quality recommends swale geometry to cover a percentage of the total impervious drainage area [54]. In summary, our review of stormwater guidelines from the Western United States reveals that there are five approaches for the sizing of bioswales [42–54]. In engineering praxis, these guidelines provide no rigorous quantitative guidance or sizing formula to address site-specific applications for bioswale designs. Thus, the design approaches based on general specifications may not meet regulatory goals for stormwater quality and quantity. Therefore, universal and reliable computational methods are of great necessity to ensure optimal and sustainable LID/BMP designs.

In theories regarding porous media flow, Darcy's law is limited to the saturated flow. Richards equation is a nonlinear partial differential equation without a general closure, which extends the Darcy's law to represent the water flow within unsaturated soils. The Richards equation includes the capillary force, converted to a form of the hydraulic head as a function of locations in a porous media. The capillary forces are usually over-emphasized, and solution methods for the Richards equation often do not converge. The CFD algorithm employed in our study is the volume of fluid (VOF) approximation, which considers averaged phase variables within a computational cell. To the best of our knowledge, the approximation level of phase separation in the Richards equation and CFD are similar regarding the functional variation for the spatial locations. Richards equation is limited to the soil domain and cannot be generally used for interfacial transport at the microscopic soil–water and soil–air boundaries unless certain mathematically particular approximations are employed. The accuracy of the CFD analysis primarily depends on the computational grid structures of VOF methods.

In academic and industrial CFD applications, OpenFOAM has been widely employed for a variety of flow modeling projects [55–57] since its initial release in 2004 [58]. We use OpenFOAM to model transport phenomena of momentum and mass within a bioswale. This paper also discusses the physical domain of the bioswale structure and how to set up an OpenFOAM case: setting up a model bioswale structure, generating bioswale meshes, specifying initial and boundary conditions, and selecting CFD solvers. We also included a brief review of modeling methods because CFD has not been extensively used for LID/BMP designs. In addition, we developed a new algorithm to more accurately investigate the two-phase transport of volatile species. Our focus is to fundamentally investigate the fast discharge of stormwater runoff with a certain pollutant concentration throughout the bioswale system.

2. Physical model and numerical solvers

2.1. Bioswale structure

Fig. 1 depicts a bioswale structure that is practiced by the Hawaii Department of Transportation (HDOT). The bioswale system is 1.8 miles (3.0 km) long and lies along Kualakai Parkway (2.7 miles [4.35 km] long) comprising of a six-lane two-way urban arterial roadway in Kapolei, Oahu, near the University of Hawaiʻi–West Oʻahu campus. The primary purpose of bioswale systems is to initially reduce stormwater runoff and partially remove non-point source pollutants, which flow from impervious urban systems such as roadways, highways, and parking lots [59]. Vegetation layers on the bioswale surface, in general, can decelerate incoming runoff flows and enhance sedimentation of suspended solids. Monitoring infiltration rates and pollutant concentration play a crucial role in the optimization of bioswale performance and also for the prolongation of the soil-matrix replacement period. Bioswales have various geometries, which include trapezoidal, rectangular, squared, and parabolic shapes. During a storm event, stormwater runoff enters the bioswale from one side of the road. Then, the stormwater runoff either infiltrates the bioswale soil zone or overflows to the overland surface. After a long duration, infiltrated water reaches the drain pipe and is discharged with pollutants of typically lower concentration than that of the runoff.

The interior soil region often consists of two layers—that is the topsoil matrix and the bottom layer. The top layer indicates the soil zone from the ground surface level to the vicinity of the embedded drain pipe. This layer should be more porous than nearby natural ground surface but sufficiently dense to maintain moderate infiltration rate through the porous media for the sake of pollutant removal. The bottom layer consists of gravel and small stones, which has higher permeability than that of the soil matrix. It mechanically supports the drain pipe and accelerates the drawdown of the infiltrated stormwater so as to allow it to discharge into the drain pipe. The drain pipe has perforations at regularly occurring intervals along the pipe length. The interstitial spaces between adjacent gravels should be large enough to allow immediate discharge to the pipe yet small enough to prevent pipe clogging due to downward migration of smaller grains.

2.2. Theoretical background

2.2.1. Fundamentals

In this section, we briefly introduce the fundamentals regarding the VOF method to perform CFD simulations for bioswale transport phenomena and explain our new solver with a modified algorithm for the transport of non-volatile solutes. The conventional VOF method deals with the two-phase flow by tracing the interfaces where physical quantities are averaged. The mass transport simulation coupled with the VOF method provides noticeable numerical diffusion at the phase-interface, especially for non-volatile solutes.

2.2.1.1. Phase averaging A two-phase flow of incompressible and immiscible fluids of air and water with specific surface tension is examined in an open atmosphere and a porous bioswale. Under the influence of gravity, the VOF

Fig. 1. Section view of a bioswale in practice along Kualakai Parkway road in Kapolei, Oahu, Hawaii.

method is used to investigate phase-averaging transport phenomena of fluids. The phase average of an arbitrary quantity, q, is defined as follows:

$$q = q_1\alpha_1 + q_2\alpha_2 \tag{1}$$

where α_i and q_i are a fraction and a value of q in phase i (1 for water and 2 for air). Because of mass conservation, the phase fractions should satisfy the following sum rule: $\alpha_1 + \alpha_2 = 1$.

2.2.1.2. Phase-averaged governing equations Due to the incompressible characteristics of water and air, the fluid velocity u satisfies the continuity equation as follows:

$$\nabla \cdot u = 0 \tag{2}$$

and the Navier–Stokes equation for momentum transport is represented using the continuum surface force model [60,61] as follows:

$$\rho\left(\frac{\partial u}{\partial t} + u \cdot \nabla u\right) = -\nabla p + \nabla \cdot T + F_s \tag{3}$$

where $\rho(\rho_1\alpha_1 + \rho_2\alpha_2)$ represents the phase-averaged fluid density and $p(P - \rho gz)$ represents the net hydrostatic pressure, which exists as the difference between the absolute pressure and the liquid-phase pressure depending on depth. F_s is the interfacial force caused due to surface tension. In Eq. (3), the viscous tensor T is given as follows:

$$T = \mu\nabla\left(u + u^t\right) \tag{4}$$

where $\mu(\mu_1\alpha_1 + \mu_2\alpha_2)$ represents the phase-averaged absolute viscosity, and superscript t indicates the transpose. The interfacial force is crucial when the boundary shape strongly depends on the capillary force, which is often solved using the standard continuum surface force model [61]:

$$F_s = \sigma\nabla \cdot \left(\frac{\nabla\alpha}{\left\|\nabla\alpha\right\|}\right)\nabla\alpha \tag{5}$$

where σ forms the surface tension at the phase boundary, for example, 0.072 N/m for air and water. In Eq. (5), α indicates the water-phase fraction (α_1), and, hereafter, the air-phase fraction will be denoted as $1 - \alpha$.

2.2.1.3. Porous media flow The porous soil zones of the bioswale are modeled using the standard Darcy flow. In this porous region, an additional force term is added on the right-hand side of Eq. (3):

$$F_d = \frac{-\rho g}{K}u = -\mu d u \tag{6}$$

where K (m/s) represents the hydraulic conductivity, d ($\rho g/\mu K$) is the Darcy constant, and g (9.81 m/s^2) constitutes the gravitational acceleration. We assume that the density of stormwater is close enough to that of pure water. Thus, the density-driven flow is assumed to not be important for our case. The hydraulic conductivity K of a fine soil has a magnitude of the order of O (10^{-5}–10^{-6}) m/s depending on the dryness of the soil zone, which yields the value of d of the order O (10^{11} –10^{12}) m^{-2}. If the fluid inertia is significant in a porous medium, one can apply the Forchheimer approach [62] as an extension of Darcy's law, but it requires the estimation of the secondary proportionality for the extra term proportional to u^2. To avoid the additional complexity due to several parameters, we restricted ourselves to the application of Darcy's flow regime, assuming that the viscous force is dominant and that the capillary force is not significant.

2.2.1.4. Pollutant transport The unsteady transport equation of the pollutant with phase-averaged concentration C can be expressed as follows:

$$\frac{\partial C}{\partial t} + \nabla \cdot \left(uC\right) = \nabla \cdot D\nabla C \tag{7}$$

where $D = D_1\alpha + D_2(1 - \alpha)$ constitutes the phase-averaged diffusivity; D_1 and D_2 represent the pollutant diffusivities within water and air phases, respectively. Typically, a solute diffusivity is considerably higher within a gas phase, when partitioned in both phases (i.e., $D_2 \gg D_1$). In principle, the governing equation (Eq. (7)) includes the pollutant diffusion even in a single phase (i.e., either $\alpha = 0$ or 1). If the volatility of the pollutant is negligible, then Eq. (7) may provide erroneous results at the phase boundaries, where α value will be of the order of O (0.1). In such a case, the phase-averaged diffusivity D can be considerably higher than D_1, and the diffusive flux from water to air phases is erroneously enhanced. This transport phenomenon is apparent, especially when the pollutant concentration in the air phase is initially zero or D_1 is small enough so that the convective pollutant transport is superior to the diffusive transport. To include interfacial reactive mass transfer, the VOF method [63] was extended as:

$$\frac{\partial C}{\partial t} + \nabla \cdot \left(uC\right) = \nabla \cdot D\nabla C - \nabla\left(D\Phi\nabla\alpha\right) \tag{8}$$

where

$$\Phi = \left(\frac{1-H}{\alpha + \left(1-\alpha\right)H}\right)C \tag{9}$$

contributes to an additional flux. Φ can be used to mimic a concentration jump at the phase boundary. An equilibrium partition of the pollutant in the two phases can be represented using Henry's law:

$$C_2 = HC_1 \tag{10}$$

where H is the dimensionless Henry constant, which is typically considerably lower than 1. No mechanism, however, is included to maintain the non-volatile pollutant within the water phase from the initial moment. To the best of our knowledge, the standard VOF method cannot describe the phase boundaries accurately using the extra-diffusion term in Eq. (8). The artificial diffusion from water to air phases can be minimized, however, by using specific parameter settings as follows. In addition to setting $C = 0$ initially in the air phase, one can forcefully set $D_2 \ll D_1$, while the inverse is true in reality. The air-phase concentration can, in principle, be further minimized by setting Henry's constant at a minimal value. By using this lower limit, the governing equation for the pollutant transport is simplified, as to minimize further the artificial diffusion,

$$\frac{\partial C}{\partial t} + \nabla \cdot \left(uC\right) = -\nabla \cdot \left(-\alpha D_1 \nabla C + C D_1 \nabla \alpha\right) \tag{11}$$

On the right-hand side of Eq. (11), the first term, $-\alpha D_1 \nabla C$, indicates the diffusive flux of the pollutant concentration, C, strictly within the water phase with an effective diffusivity αD_1. The second term, most importantly, can be interpreted mathematically as a reverse diffusion of α with an apparent diffusivity CD_1. Note that signs of $D_1 \nabla C$ and $\nabla \alpha$ are opposite of each other. An alternative interpretation of the second term exists as the reverse transport of solutes of concentration C with an effective velocity of $D_1 \nabla \alpha$. As such, the first and second terms represent solute diffusion within the water phase and the phase-boundary, respectively.

2.2.2. Model bioswale structure and mesh generation

OpenFOAM was originally developed to simulate only 3D geometries. To resolve the problem into 2D, a pseudo-3D structure needs to be generated to make pseudo front-and-back surfaces. We constructed the 3D bioswale structure of pseudo thickness of 0.4 m using an open-source mesher, Netgen [64] and exported the netgen mesh to a stereolithographic (STL) file. This STL file was employed so as to generate the OpenFOAM mesh, depicted in Fig. 2(a), using blockMesh and snappyHexMesh commands. The bioswale structure was originally prepared with an arbitrary thickness, but no mesh was generated in the direction normal to Fig. 2. The bioswale depicted in Fig. 2(a) is 3 m long from the left-most inlet to the right-most outlet and 2 m high from the bioswale bottom to the atmospheric top. Then, we added two dividers to generate refined boundaries between the atmosphere and topsoil and between the top and the bottom soil layers. Finally, all edge boundaries of the bioswale were construed as refined soil–soil interfaces. The number of divisions in the x- and y-directions was 202 and 135, respectively, which yielded equivalent grid sizes of 1.50 cm in each direction. The generated mesh has 95,498 points; 182,638 faces; and 44,963 cells; and checkMesh command was used to test the mesh's quality. The diameter of the drain pipe, presented in Fig. 2, was 30.48 cm (12 inches), located near the bottom of the bioswale. The left, right, and bottom sides of the bioswale are considered as impermeable walls, which prevent normal fluxes of momentum and mass to the wall surfaces. This assumption is considered reasonable if the soil media has higher permeability than that of the ambient soil, especially for a short-term investigation. The drain pipe contains two small holes located at 4 o'clock and 8 o'clock directions for the discharge of infiltrating water. Runoff water enters the physical domain as shown in Fig. 2(a) from the left-hand side corner with a fixed height of 5.0 cm and flows down due to gravity to the bioswale on the 5% downward slope. A stationary water column exists as a boundary condition for a stationary water source and releases water due to gravity. Actual height of the surface flow on the right ground is automatically calculated as a transient result of our CFD simulation. A large fraction of water, not infiltrated into the bioswale, overflows to the right overland surface having the same downward slope.

2.2.3. Boundary and initial conditions

Simulations were conducted for two cases: polluting and flushing. The polluting scenario indicates the storm runoff to the ideally fresh bioswale, without having water content

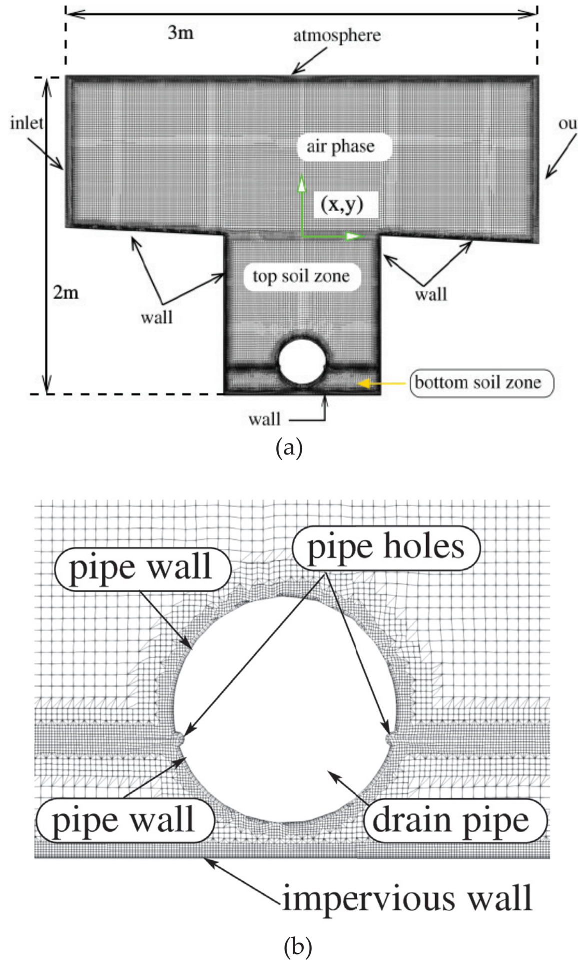

(a)

(b)

Fig. 2. Depiction of (a) pseudo-3D structure of bioswale generated by Netgen and exported to the STL format and (b) drain pipe of 30.48 cm (12 inches) diameter generated mesh using OpenFOAM tools, visualized using ParaView version 5.4 (https://www.paraview.org/). The outer length and height of the bioswale system are 3 and 2 m, respectively, and left and right ground surfaces have 5% slope.

and accumulated pollutant masses. Storm runoff containing a pollutant concentration enters the bioswale zone and infiltrates from the bioswale top into the soil and then to the drain pipe. The flushing is an opposite case, in which the bioswale is pre-contaminated with a specific concentration (assumed to be known) and the entering runoff flow has a negligible pollutant concentration. The hydrodynamic behavior within the bioswale is assumed to be very similar since the pollutant transport is a pass response to the infiltrating flow. Note that chemical and biological reactions are not included in the current study and therefore the convection–diffusion equation (Eq. (7)) can be scaled by a reference concentration (of an arbitrary choice). The flushing case was designed to understand the seemingly violating pollutant mass balance. The low-concentration infiltrating flow will sweep the pre-accumulated pollutant in general and, as a noticeable consequence, the effluent concentration is higher than the influent concentration (of the entering storm runoff). In our fundamental CFD approach, the number of physical parameters is minimized. The inflow rate into the bioswale is not an input parameter or boundary condition on the front cross-section of the bioswale (normal to the entering flow velocity), but calculated during the unsteady CFD simulations. On the bottom-left boundary 5.0 cm of water is maintained, which flows down on the slanted ground having 5% slope. In this light, we avoid using Manning's equation, which requires to input the hydraulic radius, surface slope, and surface roughness. In 2D geometry, the hydraulic radius can be easily estimated as a ratio of the normal cross-sectional area (to the incoming fluid flow) and the perimeter length wetted by the flowing fluid. Including the roughness at the macroscopic level of Manning's equation can significantly increase the computational runtime, although it is possible. If the roughness is important in a case that the surface is not smooth enough, then the slip velocity can be estimated and used as a boundary condition on the left and right ground surfaces beside the bioswale.

Specific boundary conditions and their physical implications are summarized in Table 1 and explained as follows:

2.2.3.1. Atmosphere The top surface of the computational domain shown in Fig. 2(a) indicates the ambient boundary of the stationary atmosphere. The net atmospheric pressure $p - \rho gh$ is set to zero at this boundary as a reference value because only the relative values are important in momentum transfer. U is determined as positive in the y-direction on this boundary, and its gradient normal to the atmospheric surface is zero. This is equivalent to the standard out-flow condition for the positive U. If U is determined to be inward to the air phase, then only its normal component is considered as a velocity at the boundary. In OpenFOAM, this boundary condition is implemented as pressureInletOutletVelocity. The liquid fraction α and the pollutant concentration C have the similar type of boundary conditions in the following manner. When the flow is exiting the top atmospheric boundary, gradients of α and C are set to be zero; otherwise, no additional flux of α and C are allowed. In OpenFOAM, this specific boundary condition employed for α and C is referred to as inletOutlet.

2.2.3.2. Inlet The left-most side, as shown in Fig. 2(a), is assumed to be open to the stationary ambient atmosphere and does not undergo any specific transport except for the surface runoff inflow. The inlet water height is set to 5.08 cm (2 inches), which is geometrically fixed for simplicity. At this boundary, the air velocity is set to zero, and the water velocity is set to be constant $(U_x,0,0)$, where U_x alters from 0.1 to 0.3 m/s. Although the height of the water column is fixed as 5.0 cm, the inflow water velocity as an input parameter determines the entering water velocity to bioswale surfaces. Manning's equation is a standard method used to determine the open-channel velocity as a function of slope, water height, and roughness. In contrast, the fixed height of the water column offers more flexibility to control the transient inlet flow as a boundary condition. The pressure gradient is calculated to satisfy the above-determined flow velocity. The α gradient is set to zero, and the solute concentration C is equal to $C_{\max}$ for the polluting and 0 for flushing scenarios; here, $C_{\max}$ represents the maximum pollutant concentration reasonably selected from the current literature. We selected zinc as a model pollutant with the maximum inlet concentration of 1,000.0 μg/L and the diffusivity of $D_0 = 7.024 \times 10^{-10}$ m^2/s [65,66]. Smolders and Degryse [67] investigated the fate and effect of zinc from tire debris within soils in which they reported that zinc concentrations in soil layers often reached a few hundred mg/kg. Reported zinc concentrations within 2 m of soil depth are of an order of (100) mg/kg and occasionally exceed 2,000 mg/kg [68–72]. Thus, we selected 1,000 mg/L as an extreme representative value, which does not significantly change the pollutant transport simulation since the convection is the only mechanism. In this case, the passage (or rejection) ratio of a pollutant can be used instead of the real concentration, as the

Table 1
Boundary conditions used for OpenFOAM (v4.1) simulations. Values next to the specific boundary condition names are used for specific incoming and outgoing flow conditions

Square drain mesh	$p - \rho gh$	U	α_1	C (mg/L)
Atmosphere	TotalPressure, 0	PressureInletOutletVelocity	InletOutlet, 0	InletOutlet, 0
Inlet	ZeroGradient	VariableHeightInlet	VariableHeight, (0, 1)	InletOutlet, 0
Outlet	ZeroGradient	InletOutlet, 0	InletOutlet, 0	InletOutlet, 0
Drain left	HydrostaticPressure	InletOutlet, 0	inletOutlet, 0	InletOutlet, 0
Drain right	HydrostaticPressure	InletOutlet, 0	InletOutlet, 0	InletOutlet, 0
Walls	FixedFluxPressure	No-Slip	ZeroGradient	ZeroGradient

convection–diffusion equation (Eq. (7)) can be scaled using an arbitrary (but meaningful) representative concentration value.

2.2.3.3. Outlet The right-most boundary, as shown in Fig. 2(a), allows air and water to flow naturally out of the computational domain. Normal gradients of p to this boundary are set to zero. For u, α, and C, their normal gradients are determined as zero for outgoing flow, and the values are fixed at zero for the incoming flow. In this case, the outlet boundary does not allow any incoming transport of momentum and mass.

2.2.3.4. Ground surfaces and bioswale walls The side walls of the bioswale are considered approximately impervious. At the wall boundary, the water is assumed to be not slipping and fluxes of α and C are zero, for example, $u = 0$, $\nabla\alpha = 0$ and $\nabla C = 0$. The boundary pressure p is calculated as a proper value to confirm the zero velocity at this boundary. Depending on the regulatory guidelines, the bioswale wall can be prepared as entirely impermeable to prevent any uncontrolled pollutant transfer to the environment.

2.2.3.5. Air–soil interface No boundary condition is used at the interface between the air phase and on the top bioswale. Instead, the interfacial phenomena are rigorously investigated using finer mesh layers as shown in Fig. 2(a) and seamlessly linked governing equations for the two-phase (air and water) flows. The air and heterogeneous soil regions are universally treated as a whole media having spatially-changing porosities and hydraulic conductivities (or permeabilities). In this light, the longitudinal transport normal to the top soil surface does not require a boundary condition.

2.2.3.6. Pipe surfaces and holes Fig. 2(b) shows a detailed mesh structure around the drainage pipe. The top and bottom surfaces of the circular pipe are considered as impermeable walls in contact with soil grains or water. Semi-circular extrusions on both sides of the pipe indicate fluid volumes made within the pipe holes for discharging. The top half of the drain pipe will always be filled with only air. Extruded semi-circles are used to set up the standard outflow boundary conditions for P, U, α, and C.

2.2.4. Cell zone setup

In Fig. 2, the air phase is treated as an incompressible gas phase with standard material properties of air. The soil zones of the bioswale are considered as simple porous media, characterized using the Darcy value (i.e., an inversed hydraulic permeability). For an extreme case, a high hydraulic conductivity is employed to treat an aggregate layer as a porous media using $K = 1.2$ m/s [73], which yields the Darcy constant of $d = 8.175 \times 10^6$ m^{-2}. We are interested in the highly porous soil matrix of this d-value, allowing a fast infiltration within a few minutes. As bioswale can be designed mostly for the swift discharge of initial runoff, the Darcy constant of the order $O(10^6)$ m^{-2} is too low for practical purposes. We made, therefore, the top and bottom soil zones have Darcy constant $d_t = 8.175 \times 10^8$ m^{-2} ($K = 0.12$ m/s) and $d_b = 8.175 \times 10^7$ m^{-2} ($K = 0.012$ m/s), respectively. Two pseudo-interfaces of the air-bioswale and top-bottom soil layers were prepared to accurately calculate the boundary phenomena, where P, U, α, and C are continuous anywhere within the entire computational domains. Their transports near these interfaces are, however, more complicated than those of bulk phases of air and soil. Therefore, the meshes in these zone boundaries are prepared more finely in order to accurately capture the interfacial flow patterns. We used, for the pure-phase of air and water, the densities of 1,000 and 1.21 kg/m^3, respectively, and the kinematic viscosities of 1.0×10^{-6} m^2/s and 1.51×10^{-5} m^2/s, respectively.

2.2.5. Standard and developed solvers

Users of OpenFOAM must select specific solvers that are appropriate for the problem under consideration. OpenFOAM has approximately 80 different solvers for specific applications. When required, users also can modify standard solvers to include specific phenomena. We initially began our simulation work using interFoam for an incompressible two-phase flow, which can provide an accurate simulation of coupled runoff and infiltration phenomena. To investigate non-volatile solute species (i.e., zinc in our case), we modified interFoam to generate a new solver named interPhaseDiffusionFoam, which can simulate solute transport, primarily, in the water phase without providing significant artificial diffusion. Specific algorithms are explained as follows. See Appendix section for details.

2.2.5.1. interFoam with passive transport (standard) In OpenFOAM, the phase-averaged velocity u in any phase can be calculated for the bioswale by running interFoam, and one can use a passive transport solver ScalarTransportFoam to study the convective-diffusion of the solutes. In this case, the mass transport is primarily controlled by the phase-averaged velocity U. The artificial diffusion occurs because the current version of ScalarTransportFoam treats the mass flux at the phase boundaries identically to that in a single phase. Transport phenomena of pollutants are passively calculated at each time step using only determined profiles of α and u without distinguishing phases. In summary, ScalarTransportFoam does not recognize phase boundaries and, therefore, unnecessarily enhance diffusion from the water to the air phases.

2.2.5.2. interPhaseDiffusionFoam (developed) Previously, Haroun et al. [63] developed a coupling algorithm of the VOF and solute transport by considering convection, diffusion, and volatilization of solutes. As the VOF method is based on the phase-mixing algorithm, their method requires an extremely fine computational grid for the non-volatile solute transport to eliminate the artificial diffusion. Here, we found specific theoretical approximations for non-volatile solute transfer, coupled with VOF, and described the respective terms in section 2.2.1. Details of the new and original algorithms are mathematically intense, so we include them in Appendix section.

3. Results and discussions

3.1. Distribution of infiltrating water

We test the transient flow behavior of a double-layered bioswale with an underdrain pipe in 2D space with high hydraulic conductivities to investigate the short-term transport phenomena for a rapid discharge after a heavy precipitation event. Fig. 3 depicts the initial infiltration behavior of a bioswale for the first short duration (75 s) of a precipitation event. The initial height and length of the water body are both 5.08 cm as demonstrated in the left corner of Fig. 3(a), and the flow speed is set as 0.1 m/s. After this initial moment of $t(x) = 0$, the water height is automatically adjusted based on and due to the gravity and the surface boundary condition. The top air phase and the bioswale interior are initially set as dry (represented in gray) assuming that the direct flow input from the precipitation is negligible in Fig. 3(a). The early infiltration profile is depicted in Fig. 3(b) as initiated due to gravity and the high conductivity of the topsoil. The interstitial void spaces in the bioswale soil layers are initially filled with air assumed to be incompressible in the VOF method. The top-left portion of the bioswale receives the running-off water first and then allows the water to pass through with gravitational force. The migration of the infiltrated water in the lateral direction is negligible within the soil layer. Flow inertia is fully damped in the topsoil layer, and the gravity forms the primary driving force for the infiltration at this point. Compressed air in the bioswale, due to the infiltration, generates dynamic channels for the escaping air from the porous soil layer, as depicted in Fig. 3(c). As both air and water are assumed to be incompressible, this counter-balanced transport is based on volume exchange between infiltrating water and buoyant air. As time elapses, infiltration flow patterns become uniform along the horizontal direction, but interestingly, striped horizontally. As the air initially in the soil layer is displaced to the right by the entering water from the left, its local density in the bioswale becomes higher in the runoff direction. The presence of the

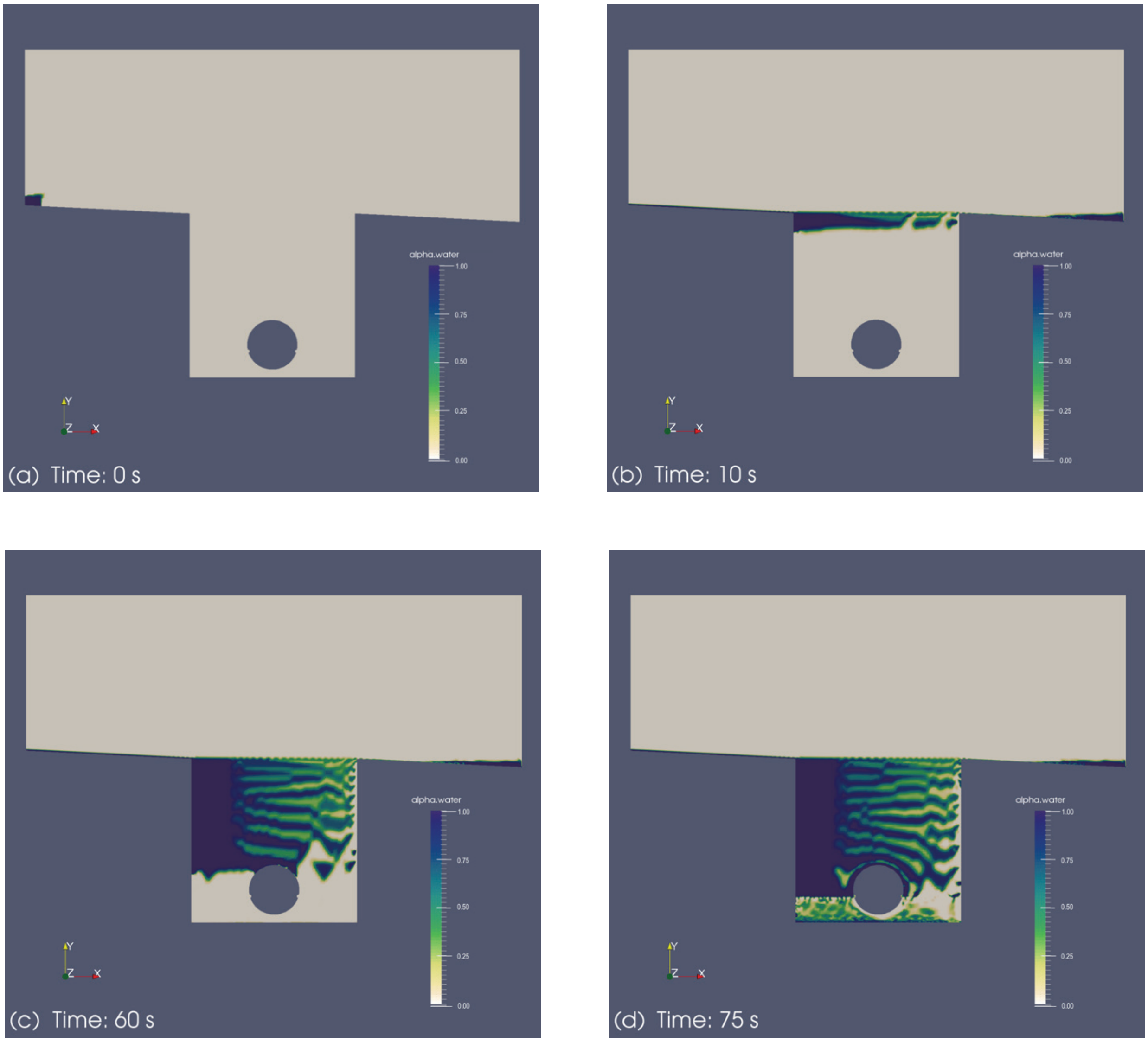

Fig. 3. Initial infiltration behavior with inflow velocity of 0.1 m/s at time (a) $t = 0$, (b) 10, (c) 60, and (d) 75 s to a bioswale.

striped distribution of air and water phases, in our opinion, is due to the limited spatial dimension of 2D space. The infiltrating flow at the inlet zone is dispersed within the bioswale. The driving force of the infiltration is gravity, hindered by the presence of soil grains. As noted previously, the downward infiltration is counter-balanced by the upward air flow, exchanging the same amount of volume occupied. In our 2D configuration, pre-existing air is pushed down by the infiltrating water and is effectively forced to move along the runoff direction on the top of bioswale. This lateral migration of air within the bioswale reduces the infiltration of water and induces the water migration in the same direction of the air migration. This distinct striped pattern must be primarily ascribed to the 2D geometry that we employed, which is practically understood by the (mathematically) infinite bioswale length along the normal direction to the cross-sectional area shown in Figs. 2–6. Fig. 3, however, clearly indicates that the distribution of infiltrating water depends on the running-off flow direction, especially when the bioswale has a high hydraulic conductivity. Since the bottom soil layer has a 10 times smaller Darcy constant, Fig. 3(d) displays rapid vertical draining near the top–bottom soil interface at the level of the pipe holes. The highly porous bottom-soil mechanically supports the pipe and provides a porous environment for the drainage flow. Due to the higher hydraulic conductivity of the bottom-soil, Fig. 3(d) displays higher water content above the top–bottom soil boundary line, passing through the drain pipe (near pipe holes). The lower water content below the top–bottom soil boundary indicates an accelerated infiltrating flow to the bottom of the bioswale. The bottom soil layer (having a higher hydraulic conductivity than that of the top-soil layer) mechanically supports the less-porous top layer and induces the fast drainage through the pipe holes. The location of the soil boundary can be set above the current boundary by reducing the low-conductivity soil zone. The partitioning of the heterogeneous soil zones can be designed based on the rain and runoff patterns to maximize the bioswale performance, which will be the topic of our next study. Partition of the top and bottom soil zones, therefore, can form an important design parameter for both the infiltration rate and for the removal of pollutants.

3.2. Effects of inflow velocity on infiltration rate

Fig. 4 compares the air–water phase distribution at $t = 60$ s for three inflow velocities, having Darcy values equal to those of Fig. 3. For specific comparison, we put Fig. 3(a) as identical to Fig. 4(a) having an inflow velocity of 0.1 m/s. We observed that the striped pattern disappeared in Figs. 4(b) and (c) for higher inflow velocities of 0.2 and 0.3 m/s, respectively.

Due to the larger amount of running-off water on the topsoil surface, the infiltrating water volume is considerably lesser than that of the laterally migrating runoff on the bioswale surface. Water distribution profiles of Figs. 4(b) and (c) appear similar to each other. Thus, this similarity implies that the infiltration velocity is almost independent from runoff velocity (if the runoff velocity is sufficiently fast), but the counter-flow of the air is ubiquitous. This, in practical terms, indicates that the high-conductivity bioswale must have a minimum threshold running-off velocity that generates the spatially uniform infiltration pattern. Below the threshold value, the bioswale must exhibit lesser symmetric infiltration patterns along the central vertical axis. In all cases, the phenomena of volume exchanges between the air and water phases control the distribution of the infiltrating water under the initial runoff effect on a dry bioswale. Now, Fig. 5 provides a closer view of the porous topsoil zone from Fig. 4, where the runoff water starts infiltrating due to gravity. The slower infiltration speed is due to a higher Darcy value of the topsoil. The water distribution of the slowest inflow velocity of 0.1 m/s, shown in Fig. 5(a), contains a wavy pattern, which is due to

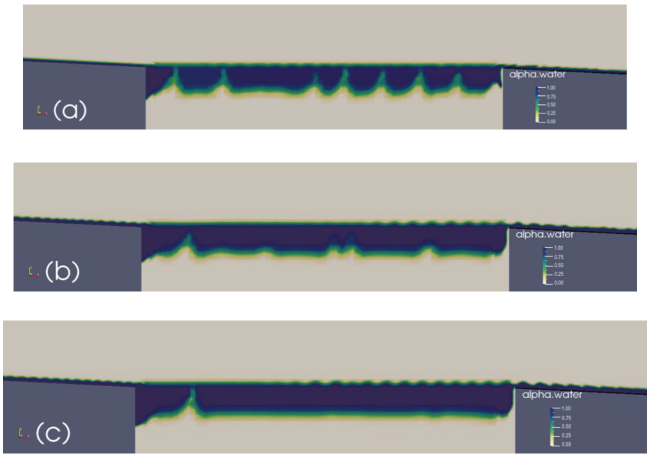

Fig. 5. Closer visual investigation of infiltrating water distribution at $t = 60$ s to topsoil layer. Runoff velocities of (a), (b), and (c) are equal to those of Fig. 4.

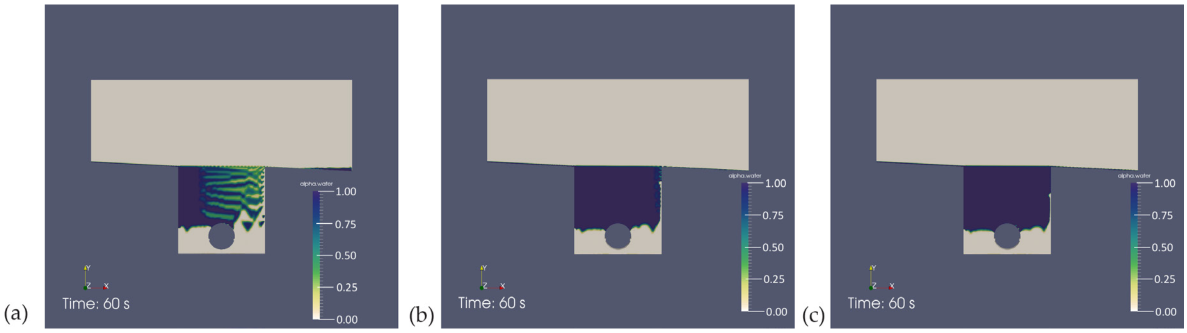

Fig. 4. Snapshots of infiltrating water distribution at $t = 60$ s to topsoil layer with inflow velocities of (a) 0.1, (b) 0.2, and (c) 0.3 m/s. The two holes of the drain pipe are open.

the intermediate air back-flow to compensate for the amount of water infiltration. This pattern gradually disappears as the inflow velocity increases to 0.2 and 0.3 m/s, shown in Figs. 5(b) and (c), respectively. Air backflow was observed in two locations, including one near the bioswale inlet and the other at the right outlet. In summary, the three running-off velocities do not change the infiltration depth shortly after the infiltration begins. This supports our previous observation from Fig. 4, the infiltration speed and the depth are insensitive to the running-off velocity. Being consistent with the implication from Fig. 4, only high conductivity changes the infiltration patterns, regardless of the runoff velocity.

3.3. Effects of pipe hole on the water–air phase distribution

Unlike conventional approaches that assume the stationary fluid at the porous media interface, our CFD approach links the fast overland flow and the infiltration flow by introducing small enough time interval of the CFD simulation. Fig. 6 depicts the infiltration streamlines of (a) open and (b) closed pipes. For simplicity, we included the infiltration simulation results of Fig. 3(a) as Fig. 6(a) for open pipe holes, and Fig. 6(b) shows streamlines of closed pipe holes. In actuality, the pipe holes are periodically located at every 30–60 cm along the pipe. As our simulations are restricted to 2D space for a qualitative analysis with fast computation, the size of pipe hole represents its averaged diameter along the longitudinal direction of the drain pipe. Alternatively, the open and closed pipe hole cases of Figs. 6(a) and (b) can be understood as two cross-sections of the bioswale at different locations, one passing through the pipe holes and the other in the middle of the two periodic holes in the longitudinal direction. In the real 3D sub-surfaces of the bioswale, these flow patterns must be periodically mixed depending on the averaged length between two adjacent holes along the drainage direction. Periodically located circular holes will create heterogeneous flow patterns above them since the infiltrating flow will experience the pressure gradient toward the holes from locations above them. If there is no significant driving force to the fluid along the pipe direction, then the flow pattern must also be periodic at the repetitive hole locations. Averaging the flow patterns between two adjacent holes in 3D is equivalent to creating a smaller hole in our 2D configuration, having the same area for water penetration. The equivalent hole size in 2D is calculated as a void area of a real 3D hole divided by the nearest distance between two adjacent holes in 3D. The streamlines in Fig. 6(a) demonstrate simple vertical pathways of the mixed phase fluid. The streamlines are shown as smooth and continuous because the bioswale is modeled as a uniform porous media. Note that these streamlines do not individually express the pathway of air and water but represent phase-averaged flow paths. Because the pipe holes are also pressure outlets, the apparent compression of air phase due to the infiltrating water is less significant than that observed in Fig. 6(b). Two vertical columns are observed in Fig. 6(b) through which air flows upward to reduce the gas-phase pressure (represented by a reddish color). In OpenFOAM, the pressure of incompressible fluids is calculated as the actual pressure divided by the constant fluid density to take advantage of computational efficiency. The initial air phase of the closed pipe case is either trapped between down-coming water bodies or flowing upward through homogeneous void spaces. Based on our findings, Fig. 6 implies that a considerable number of pipe holes may reduce the local compression of air and hence minimize the infiltration resistance due to the counter-balancing air flow. This trend can be limited to the soil matrixes of high permeability, but the air backflow cannot be ignored in mass transport phenomena within the porous bioswale. Finally, we found that a dynamic pattern of air distribution can be partially controlled by the geometrical characteristics of the pipe holes.

3.4. Pollutant transport

We simulate the flushing of a partially dry bioswale as a maintenance strategy to washout the pollutant buildup. The mass flux of zinc is calculated as the concentration multiplied by the outgoing flow velocity through a pipe hole (i.e., $J = Cu$). It is assumed that a $t = 0$, the bottom soil layer has $\alpha = 1$ and $C = 1{,}000$ μg/L, and the topsoil layer contains $\alpha = 0.5$ and $C = 500$ μg/L. Fig. 7 represents the transient mass fluxes in the x- and y-directions at both the left and right holes. The initial

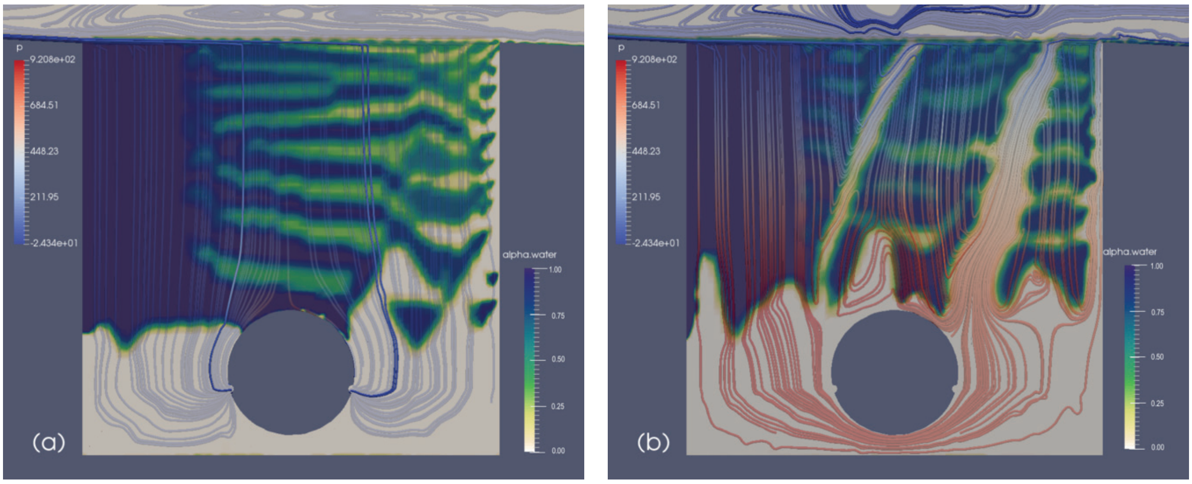

Fig. 6. Snapshots show the effects of pipe holes on the infiltration patterns, where pipe holes are (a) open and (b) closed. The color of streamlines indicates the intensity of the pressure in the bioswale.

discharge flux to the left hole J_x decreases rapidly in 10 s due to the gravity-driven flow of water existing in the interstitial spaces. The right J_x shows a symmetric pattern to the left J_x having an opposite direction of the negative sign. The left and right J_x has a mean and standard deviation values of 162.45 ± 19.14 and –152.43 ± 18.15, respectively. A closer investigation shows that the left J_x has a higher magnitude than the right J_x. This result may be explained by the fact that infiltration starts at the left inlet on the top surface of a high conductivity. Furthermore, the difference of J_x in the left and right holes may be attributed to the infiltrating water displaced by the air from the left into the right holes, as confirmed in Figs. 3 and 4. The initial infiltration of runoff at the left-top corner of the bioswale surface causes two distinct effects. First, until the bioswale is fully saturated, water content (α) as a decreasing trend along the surface runoff direction. Second, this spatially biased infiltration pushes pre-existing air within the bioswale along the same lateral direction, and, as a feedback, the pressurized air provides hydraulic resistance to the lateral flow. Third, a fraction of pressurized air reaches the right wall and flows up due to the buoyant force. Overall, the infiltration on the left-top surface is balanced with the escaping air-flow on the right-top surface. The restricted 2D configuration prevents the air and water movements in the normal direction to the runoff (i.e., the pipe-aligned direction). The coupled transport of air and water generates the biased drainage of infiltrated water to the pipe holes. If the bioswale is initially fully saturated, then the magnitude difference of J_x of the opposite-sided holes must be negligible. J_y values for both holes fluctuate near zero but their average values are positive. This is because the holes are positioned at 4 o'clock and 8 o'clock directions, and their normal surfaces are slightly directed upward. We observe that when the J_y increases temporarily, J_x decreases. This rather unexpected finding might be a result of the transport across the holes that water discharge and air flows are counter-balanced. This flushing scenario shows that the bioswale can gradually discharge pre-accumulated pollutants. Flushing could be used as a maintenance strategy for the gradual or intermittent release of contaminants below a specific concentration during dry periods.

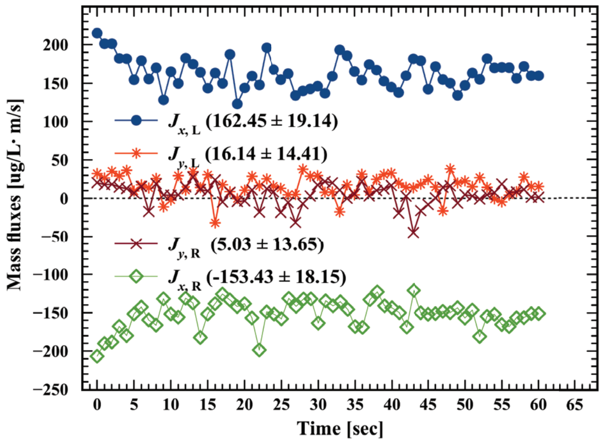

Fig. 7. Pollutant flux components in x- and y-direction through the left (L) and right (R) pipe holes.

4. Conclusions

CFD simulations have been carried out to investigate coupled transport in a bioswale using OpenFOAM version 4.1. This current study applies a computational approach to simulate the initial infiltration trend with several conditions of the running-off to a dual-media bioswale with a drain pipe. Our work has several noteworthy features as follows.

First, the current study is, to the best of our knowledge, the first CFD application on bioswale design and performance by the seamless coupling of overland and infiltrating water flows. For the early-stage infiltration of stormwater, a threshold value of the runoff velocity exists, above which the infiltrated water is uniformly distributed and below which the distribution is wavy. For a fast runoff above high conductivity bioswale, the soil zone induces asymmetric water patterns along the runoff direction. Second, a slow runoff velocity yields a wavy profile of the down-coming waterfront, which gradually disappears as the running-off velocity increases. This flow behavior must be partially ascribed to the 2D nature of the simulations, but it emphasizes the reverse flow of air during the initial infiltration to the unsaturated bioswale. Third, the presence of the pipe holes indicates the unique behavior of air dynamics inside the bioswale. When the pipe holes are closed (or clogged), the air-phase pressure increases due to the going-down water volume, and vertical void columns form for air flow channeling. To thoroughly understand the interaction between infiltrating and escaping water flows, 3D CFD modeling is of great necessity, especially in the initial infiltration stage. Fourth, we would like to emphasize that a new solver, interPhaseDiffusionFoam, was successfully developed to simulate the non-volatile pollutant transport in separate phases at different time scales. While the VOF method deals with only the phase-averaged quantities, the new solver employed an algorithmic approximation based on physical interpretation and offered a closer mimicking of the pollutant diffusion in the two-phase flow.

Finally, we emphasized a need for universal and reliable computational methods, which can be used to determine dimensions of bioswales. Note that current bioswale sizing guidelines lack consistency. Our current work is limited to qualitative analyses of short-term and rapid-flow behaviors of highly porous 2D bioswales because experimental verification is an additional arduous task. These results, however, have significant potential implication in the early-stages conceptual design and analysis of bioswales for better efficiency and stable maintenance. By having historical runoff data and thorough understanding of precipitation patterns, one can control the time required to fully saturate a bioswale, depending on the periodicity of storm events. Subsequently, CFD analysis can suggest optimal combinations of physical dimensions, hydraulic conductivities, thicknesses of the dual (or even triple) soil layers, as well as the locations and sizes of the drain pipes and perforated holes. Further modeling work is required to develop sizing formulas to ensure optimal hydraulic performance. Long-term transport studies of the bioswale would be beneficial to holistically understand in 3D the physico-chemical/biological reactions of multiple pollutants in unsteady porous-media flow fields.

Acknowledgments

This work was also supported by the Kohala Center of Hawaiian Scholars Doctoral Fellowship Program (formerly known as the Mellon-Hawaiʻi Doctoral and Postdoctoral Fellowship Program), the Deviants from the Norm Fund and Dr. Paul and Elizabeth Nakayama for the first author. The authors would like to thank Mr. Curtis Matsuda at the Hawaii Department of Transportation for his inspiring discussions. This research used the Extreme Science and Engineering Discovery Environment (XSEDE), which is supported by National Science Foundation grant number ACI-1053575.

References

[1] R.A. McManamay, S.S. Nair, C.R. DeRolph, B.L. Ruddell, A.M. Morton, R.N. Stewart, M.J. Troia, L. Tran, H. Kim, B.L. Bhaduri, US cities can manage national hydrology and biodiversity using local infrastructure policy, PNAS, 1140 (2017) 9581–9586.
[2] C.B. d'Amour, F. Reitsma, G. Baiocchi, S. Barthel, B. Güneralp, K. Erb, H. Haberl, Felix Creutzig, K.C. Seto, Future urban land expansion and implications for global croplands, PNAS, 1140 (2016) 8939–8944.
[3] Z. Zhang, N.E. Zimmermann, A. Stenke, X. Li, E.L. Hodson, G. Zhu, C. Huang, B. Poulter, Emerging role of wetland methane emissions in driving 21st century climate change, PNAS, 1140 (2017) 9647–9652.
[4] J. Franczy, H. Chang, The effects of climate change and urbanization on the runoff of the Rock Creek basin the Portland metropolitan area, Oregon, USA, Hydrol. Processes, 23 (2009) 805–819.
[5] J.M. Hathaway, W.F. Hunt, R.M. Guest, D.T. McCarthy, Residual indicator bacteria in autosampler tubing: a field and laboratory assessment, Water Sci. Technol., 690 (2014) 1120–1126.
[6] Z. Zahmatkesh, S. Burian, M. Karamouz, H. Tavakol-Davani, E. Goharian, Low-impact development practices to mitigate climate change effects on urban stormwater runoff: case study of New York City, J. Irrig. Drainage Eng., 1410 (2015) 1–13.
[7] J. Xie, H. Chen, Z. Liao, X. Gu, D. Zhu, Environmental Modelling and Software an integrated assessment of urban flooding mitigation strategies for robust decision making, Environ. Model. Software, 95 (2017) 1364–8152.
[8] US EPA, Developing Your Stormwater Pollution Prevention Plan A Guide for Construction Sites, Technical Report, Washington D.C., 2007.
[9] M.A. Benedict, E.T. McMahon, Green Infrastructure: Smart Conservation for the 21st Century, Sprawl Watch Clearinghouse Monograph Series, 2000.
[10] G.D. Geldof, Coping with uncertainties in integrated urban water management, Water Sci. Technol., 360 (1997) 265–269.
[11] V.G. Mitchell, Applying integrated urban water management concepts: a review of Australian experience, Environ. Manage., 370 (2006) 589–605.
[12] D. Barlow, G. Burrill, J.R. Nolfi, A Research Report on Developing a Community Level Natural Resource Inventory System, Center for Studies in Food Self-Sufficiency, Vermont Institute of Community Involvement, Burlington, VT, 1977.
[13] L.S. Coffman, Low-Impact Development design: A New Paradigm for Stormwater Management Mimicking and Restoring the Natural Hydrologic Regime an Alternative Stormwater, Prince George's County Department of Environmental Resources Maryland County, USA, 2000.
[14] US EPA, Low Impact Development (LID) A Literature Review, Technical Report, United States EPA Office of Water, Washington D.C., 2000.
[15] N. Chang, Hydrological Connections between low-impact development, watershed best management practices, and sustainable development, J. Hydrol. Eng., 150 (2010) 384–385.
[16] M. Ignatieva, C. Meurk, G. Stewart, Low Impact Urban Design and Development (LIUDD): matching urban design and urban ecology, Landscape Rev., 120 (2008) 61–73.
[17] C.J. Pratt, A review of source control of urban stormwater runoff, Water Environ. J., 9 (1995) 132–139.
[18] P. Hamel, E. Daly, T.D. Fletcher, Source-control stormwater management for mitigating the impacts of urbanisation on baseflow: a review, J. Hydrol., 485 (2013) 201–211.
[19] A.R. Cizek, W.F. Hunt, Defining predevelopment hydrology to mimic predevelopment water quality in stormwater control measures (SCMs), Ecol. Eng., 57 (2013) 40–45.
[20] G. Blecken, W.F. Hunt III, A.M. Al-Rubaei, M. Viklander, W.G. Lord, Stormwater Control Measure (SCM) maintenance considerations to ensure designed functionality, Urban Water J., 14 (2017) 278–290.
[21] M.A. Kachchu Mohamed, T. Lucke, F. Boogaard, Preliminary investigation into the pollution reduction performance of swales used in a stormwater treatment train, Water Sci. Technol., 690 (2014) 1014–1020.
[22] S.M. Charlesworth, C.A. Booth, Sustainable Surface Water Management: A Handbook for SuDs, Wiley-Blackwell, Published in West Sussex, United Kingdom, 2017.
[23] D. Butler, J. Parkinson, Towards sustainable urban drainage, Water Sci. Technol., 35 (1997) 53–63.
[24] CIRIA, Sustainable Urban Drainage Systems Design Manual for Scotland and Northern Ireland, Technical Report, Published by "Construction Industry Research and Information Association", London, United Kingdom, 2000.
[25] Victorian Stormwater Committee, Urban stormwater best practice environmental management guidelines, CSIRO Publishing, Melbourne, Australia, 1999.
[26] S.D. Lloyd, T.H.F. Wong, C. Chesterfield, Water Sensitive Urban Design–A Stormwater Management Perspective, Industry Report, Cooperative Research Centre for Catchment Hydrology, Monash University, Victoria, Australia, 2002.
[27] P.J. Morison, R.R. Brown, C. Cocklin, Transitioning to a waterways city Municipal context, capacity and commitment, Water Sci. Technol., 620 (2010) 162–171.
[28] P. Abbott, J. Davies, P. Simkins, P. Morgan, C. Levin, D. Robinson, Creating Water Sensitive Places: Scoping the Potential for Water Sensitive Urban Design in the UK, CIRIA Publishing, London, 2013.
[29] T.D. Fletcher, W. Shuster, W.F. Hunt, R. Ashley, D. Butler, S. Arthur, S. Trowsdale, S. Barraud, A. Semadeni-Davies, J. Bertrand-Krajewski, P.S. Mikkelsen, G. Rivard, M. Uhl, D. Dagenais, M. Viklander, SUDS, LID, BMPs, WSUD and more–the evolution and application of terminology surrounding urban drainage, Urban Water J., 120 (2015) 525–542.
[30] K. Eckart, Z. McPhee, T. Bolisetti, Performance and implementation of low impact development: a review, Sci. Total Environ., 607 (2017) 413–432.
[31] C.A. Zimmer, I.W. Heathcote, H.R. Whiteley, H. Schroeter, Low impact development practices for stormwater: implications for urban hydrology, Can. Water Res. J., 320 (2007) 193–212.
[32] S.D. Lloyd, T.H.F. Wong, B. Porter, The planning and construction of an urban stormwater management scheme, Water Sci. Technol., 450 (2002) 1–10.
[33] N. Bastien, S. Arthur, S. Wallis, M. Scholz, The best management of SuDS treatment trains: a holistic approach, Water Sci. Technol., 610 (2010) 263–272.
[34] N.R.P. Bastien, S. Arthur, S.G. Wallis, M. Scholz, Runoff infiltration, a desktop case study, Water Sci. Technol., 630 (2011) 2300–2308.
[35] X. Zhang, X. Guo, M. Hu, Hydrological effect of typical low impact development approaches in a residential district, Nat. Hazards, 800 (2016) 389–400.
[36] C. Pyke, M.P. Warren, T. Johnson, J. Lagro, J. Scharfenberg, P. Groth, R. Freed, W. Schroeer, E. Main, Landscape and urban planning assessment of low impact development for managing stormwater with changing precipitation due to climate change, Landscape Urban Plan., 1030 (2011) 166–173.
[37] V. Pappalardo, D. La Rosa, A. Campisano, P. La Greca, The potential of green infrastructure application in urban runoff control for land use planning: a preliminary evaluation from a southern Italy case study, Ecosyst. Serv., 260 (2017) 345–354.

[38] H. Jia, Y. Lu, S.L. Yu, Y. Chen, Planning of LID–BMPs for urban runoff control: the case of Beijing Olympic village, Sep. Purif. Technol., 84 (2012) 112–119.

[39] J. Gao, R. Wang, J. Huang, M. Liu, Application of BMP to urban runoff control using SUSTAIN model: case study in an industrial area, Ecol. Model., 318 (2015) 177–183.

[40] L.M. Ahiablame, B.A. Engel, I. Chaubey, Effectiveness of low impact development practices: literature review and suggestions for future research, Water Air Soil Pollut., 2230 (2012) 4253–4273.

[41] H. Rujner, G. Leonhardt, J. Marsalek, M. Viklander, High-resolution modelling of the grass swale response to runoff inflows with Mike SHE, J. Hydrol., 562 (2018) 411–422.

[42] State of Hawaii Office of Planning, Coastal Zone Management Program, Hawaii Low Impact Development, A Practitioner's Guide, Technical Report, 2006.

[43] Alaska Department of Environmental Conservation, Alaska Storm Water Guide, Division of Water, Anchorage, Alaska, Technical Manual, 2011.

[44] Arizona Department of Transportation, Erosion and Pollution Control Manual for Highway Design and Construction, Technical Manual, 2012.

[45] Las Vegas Valley Stormwater Quality Management Committee and Clark County regional Flood Control District, Las Vegas Valley Construction Site Best Management Practices Guidance Manual, Las Vegas, Nevada, Technical Manual, 2009.

[46] City and County of Honolulu, Department of Planning and Permitting, Storm Water BMP Guide for New and Redevelopment, Technical Report, 2017.

[47] New Mexico State Highway and Transportation Department, Drainage Manual Volume 1, Hydrology, Technical Manual, 1995.

[48] Utah Department of Transportation, UDOT Stormwater Quality Design Manual, Technical Manual, 2018.

[49] Prince George's County, Design Manual for Use of Bioretention in Storm Water Management, PGC, Maryland, Department of Environmental Services, Technical Manual, 1993.

[50] State of Washington, Stormwater Management Manual for Western Washington, Department of Ecology, Technical Manual, 2012.

[51] State of Oregon, Department of Environmental Quality, Biofilters (Bioswales, Vegetative Buffers, & Constructed Wetlands) For Storm Water Discharge Pollution Removal: Guidance for using Bioswales, Vegetative Buffers, and Constructed Wetlands for Reducing, Minimizing, or Eliminating Pollutant Discharges to Surface Water, Technical Manual, 2003.

[52] California Stormwater Quality Association, Stormwater Best Management Practice Handbook: New Development and Redevelopment, Technical Manual, 2003.

[53] City of Austin, TX, Design Guidelines for Water Quality Control Basins, Public Works Department of Austin, Texas, Technical Manual, 1996.

[54] Idaho Department of Environmental Quality, Catalog of Stormwater Best Management Practices for Idaho Cities and Counties, Technical Manual, 2005.

[55] OpenFoam, Open FOAM The Open Source CFD Toolbox Programmer's Guide, 2017.

[56] R. Gjesing, J. Hattel, U. Fritsching, Coupled atomization and spray modelling in the spray forming process using OpenFoam, Eng. Appl. Comput. Fluid Mech., 3 (2009) 471–486.

[57] H. Jasak, OpenFOAM: Open source CFD in research and industry, 10 Int. J. Naval Arch. Ocean Eng., 30 (2009) 89–94.

[58] P. Higuera, J.L. Lara, I.J. Losada, Three-dimensional interaction of waves and porous coastal structures using OpenFOAM Part I: Formulation and validation, Coastal Eng., 83 (2014) 243–258.

[59] Hawaii Department of Transportation, Plans for Kaneohe Water Shed Strom Water Best Management Practices on Oahu, Technical Report, Honolulu, Hawaii, 2014.

[60] C.W. Hirt, B.D. Nichols, Volume of fluid (VOF) method for the dynamics of free boundaries, J. Comput. Phys., 390 (1981) 201–225.

[61] J.U. Brackbill, D.B. Kothe, C. Zemach, A continuum method for modelling surface tension, J. Comput. Phys., 1000 (1992) 335–354.

[62] A. Bejan, Convection Heat Transfer, John Wiley & Sons Inc., Hoboken, New Jersey, 4th ed., 2013.

[63] Y. Haroun, D. Legendre, L. Raynal, Volume of fluid method for interfacial reactive mass transfer: application to stable liquid film, Chem. Eng. Sci., 650 (2010) 2896–2909.

[64] J. Schöberl, C++11 Implementation of Finite Elements in NGSolve, ASC Report, 2014.

[65] H.S. Harned, R.M. Hudson, The diffusion coefficient of zinc sulfate in dilute aqueous solution at 25°C, J. Am. Chem. Soc., 730 (1951) 3781–3783.

[66] S.F. Patil, A.V. Borhade, M. Nath, Diffusivity of some zinc and cobalt salts in water, J. Chem. Eng. Data, 380 (1993) 574–576.

[67] E. Smolders, F. Degryse, Fate and effect of zinc from tire debris in soil, Environ. Sci. Technol., 36 (2002) 3706–3710.

[68] R.D. Post, A.N. Beeby, Microbial biomass in suburban roadside soils: estimates based on extracted microbial C and ATP, Soil Biol. Biochem., 25 (1993) 199–204.

[69] R. Garcia, E. Millán, Assessment of Cd, Pb, and Zn contamination in roadside soils and grasses from Gipuzkoa (Spain), Chemosphere, 37 (1998) 1615–1625.

[70] P.K. Lee, J.C. Touray, Characteristics of polluted artificial soil located along a motorway and effects of acidification on the leaching behavior of heavy metals (Pb, Zn, Cd), Water Res., 32 (1998) 3425–3435.

[71] A.C. Norrstrom, G. Jacks, Concentration and fractionation of heavy metals in roadside soils receiving de-icing salts, Sci. Total Environ., 218 (1998) 161–174.

[72] C. Pagotto, N. Remy, M. Legret, P. Le Cloirec, Heavy metal pollution of road dust and roadside soil near a major rural highway, Environ. Technol., 22 (2001) 307–319.

[73] P. Murphy, N.B. Kaye, A.A. Khan, Hydraulic performance of aggregate beds with perforated pipe underdrains flowing full, J. Irrig. Drainage Eng., 140 (2014) 1–7.

[74] A.S. Kim, J.L. Irvine, interPhaseDiffusionFoam. 2018. Available at: https://github.com/enphysoft/interPhaseDiffusionFoam.

Appendix

A1. A modified VOF algorithm with mass transfer

The mass conservation for the local concentration $C_k(r,t)$ in a phase k (1 for liquid [water] and 2 for gas [air]) is as follows:

$$\frac{\partial C_k}{\partial t} + \nabla \cdot \left(U_k C_k\right) = -\nabla \cdot J_k \tag{A1}$$

where U_k and J_k are the local fluid velocity and diffusive flux of pollutants, respectively. The diffusive flux J_k is assumed to follow Fick's law of diffusion:

$$J_k = -D_k \nabla C_k \tag{A2}$$

where D_k is a diffusivity constant. If a cell volume of a computational grid contains both the liquid and gas phases, Eqs. (A1) and (A2) are to be averaged within the cell volume. The following equation shows that a fraction of phase k is defined as a ratio of the volume and the total cell volume:

$$\alpha_k = \frac{V_k}{V_c} \tag{A3}$$

An average quantity of an arbitrary physical variable q in the cell volume is as follows:

$$q = \frac{1}{V_c}\int_{V_c} q\,dV = \sum_k \alpha_k \bar{q}_k = \alpha_1 \bar{q}_1 + \alpha_2 \bar{q}_2 \tag{A4}$$

where

$$\bar{q}_k = \frac{1}{V_k}\int_{V_k} q\,dV \tag{A5}$$

is an average of q (only) in phase k. If Eq. (A1) is averaged along the overall cell volume. Thus, we have the following expression:

$$\frac{\partial \alpha_k \overline{C_k}}{\partial t} + \nabla \cdot \left(\alpha_k \overline{U_k C_k}\right) = -\nabla \cdot \alpha_k \overline{J_k} \tag{A6}$$

Now, we make a sum of each side of Eq. (A6) with respect to k from 1 to 2, which leads to:

$$\frac{\partial C}{\partial t} + \nabla \cdot UC = -\nabla \cdot J \tag{A7}$$

where

$$C = \alpha_1 \overline{C_1} + \alpha_2 \overline{C_2} \tag{A8}$$

$$UC \simeq \overline{UC} = \alpha_1 \overline{U_1 C_1} + \alpha_2 \overline{U_2 C_2} \tag{A9}$$

Similarly, the average flux is defined as $J = \sum_{k=1}^{2} \alpha_k \overline{J_k}$, but if this definition is applied, J cannot be represented using the cell-volume averaged quantities. An approximation using the averaged diffusivity is applied to both the liquid and gas as follows:

$$J \simeq -D\left[\alpha_1 \nabla C_1 + \alpha_2 \nabla C_2\right] \tag{A10}$$

where the mean diffusivity is calculated as a phase-average

$$D = \alpha_1 D_1 + \alpha_2 D_2. \tag{A11}$$

For simplicity, we omit the subscript 1 for α and replace α_2 by $1 - \alpha$. At the phase boundary, the pollutant partition between the two phases can be approximated using Henry's law (i.e., $C_2 = HC_1$), where H forms a dimensionless Henry's constant. The mean flux J is represented as follows:

$$J = -D\left[\nabla C - \Phi \nabla \alpha\right] \tag{A12}$$

using a mathematical identity $\alpha_1 \nabla C_1 = \nabla[\alpha_1 C_1] - C_1 \nabla \alpha$. The final governing equation using the volume average is Eq. (8), having the effective convective transport controlled by the average phase velocity U.

A2. Additional treatment

Unless solutes are volatile, mass transport between the liquid–gas interface is negligible. In this case, parameters should be appropriately selected to entirely prevent the interfacial diffusive transport. The diffusivity within a gas phase is approximately 10^3–10^4 times higher than that within a liquid phase. In this case, Eq. (A11) may not represent an appropriate estimation approach so as to maintain solute molecules in the liquid phase, minimizing the pollutant transfer to the gas phase.

If the gas phase concentration C_2 is initially zero, then there should not be any mass transfer from the liquid phase, and C_2 should be maintained as zero. The VOF method fails to include the solute diffusion in two separate phases using the phase-averaged diffusivity. To mathematically implement this real phenomenon in our CFD simulations, we used an arbitrarily forceful assumption

$$\frac{D_2}{D_1} \approx \frac{C_2}{C_1} = H \ll 1 \tag{A13}$$

which is similar to original Henry's law. Then, for small values of H, we calculated

$$D = D_1\left(\alpha + \left(1 - \alpha\right)H\right) \to \alpha D_1 \tag{A14}$$

and most importantly,

$$D\Phi = D_1\left(1-H\right)C \rightarrow D_1C \tag{A15}$$

Therefore, we have

$$\begin{aligned}\frac{\partial C}{\partial t} + \nabla\cdot UC &= \nabla\left(D_1\alpha\nabla C\right) - \nabla\left(D_1C\nabla\alpha\right)\\ &= D_1\nabla\left(\alpha\nabla C - C\nabla\alpha\right)\end{aligned} \tag{A16}$$

where $D_1\nabla(\alpha\nabla C)$ indicates the diffusive flux with a diffusivity D_1 weighted by the liquid fraction α, and $-D_1C\nabla$ implies back transport of α from the gas phase to the liquid phase. This diffusion coefficient of α is conceptually determined as CD_1. This solver is named interPhaseDiffusionFoam and available online [74].